

Supporting Information:

Ultrafast Laser-Induced Isomerization Dynamics

In Acetonitrile

Matteo McDonnell,^{*,†} Aaron C. LaForge,^{*,†} Juan Reino-González,[‡] Martin Disla,[†] Nora G. Kling,[†] Debadarshini Mishra,[†] Razib Obaid,[†] Margaret Sundberg,[†] Vít Svoboda,[¶] Sergio Díaz-Tendero,^{*,‡,§,||} Fernando Martín,^{*,‡,§,⊥,#} and Nora Berrah^{*,†}

[†]*Department of Physics, University of Connecticut, Storrs, Connecticut, 06269, USA*

[‡]*Departamento de Química, Módulo 13, Universidad Autónoma de Madrid, 28049 Madrid, Spain, EU*

[¶]*Laboratory of Physical Chemistry, ETH-Zürich, 8093 Zürich, Switzerland*

[§]*Condensed Matter Physics Center (IFIMAC), Universidad Autónoma de Madrid, 28049 Madrid, Spain, EU*

^{||}*Institute for Advanced Research in Chemical Sciences(IAdChem), Universidad Autónoma de Madrid, 28049 Madrid, Spain, EU*

[⊥]*Instituto Madrileño de Estudios Avanzados en Nanociencia (IMDEA-Nano), Campus de Cantoblanco, 28049 Madrid, Spain, EU*

[#]*Donostia International Physics Center (DIPC), Paseo Manuel de Lardizabal 4, 20018 Donostia-San Sebastián, Spain, EU*

E-mail: matteo.mcdonnell@uconn.edu; aaron.laforge@uconn.edu; sergio.diaztendero@uam.es; fernando.martin@uam.es; nora.berrah@uconn.edu

Coulomb Explosion Imaging

We track the isomerization and fragmentation reactions in acetonitrile (CH_3CN) using Coulomb explosion imaging (CEI) via a laser pump-probe scheme to time-resolve the observed processes. Fig. S1, panel (a), depicts the general scheme of the CEI technique while panel (b) illustrates the energy diagram for acetonitrile molecule - H-dissociation (loss), isomerization and fragmentation- in the cationic molecule before double ionization. The fragmentation dynamics scenarios of the singly charged CH_3CN lead to H and H_2 loss, NHM, SHM and DHM, as discussed in the main text. Relative energies for the exit channels are given with respect to the neutral CH_3CN , and were computed at the DFT-B3LYP/6-31++G(d,p) level of theory.

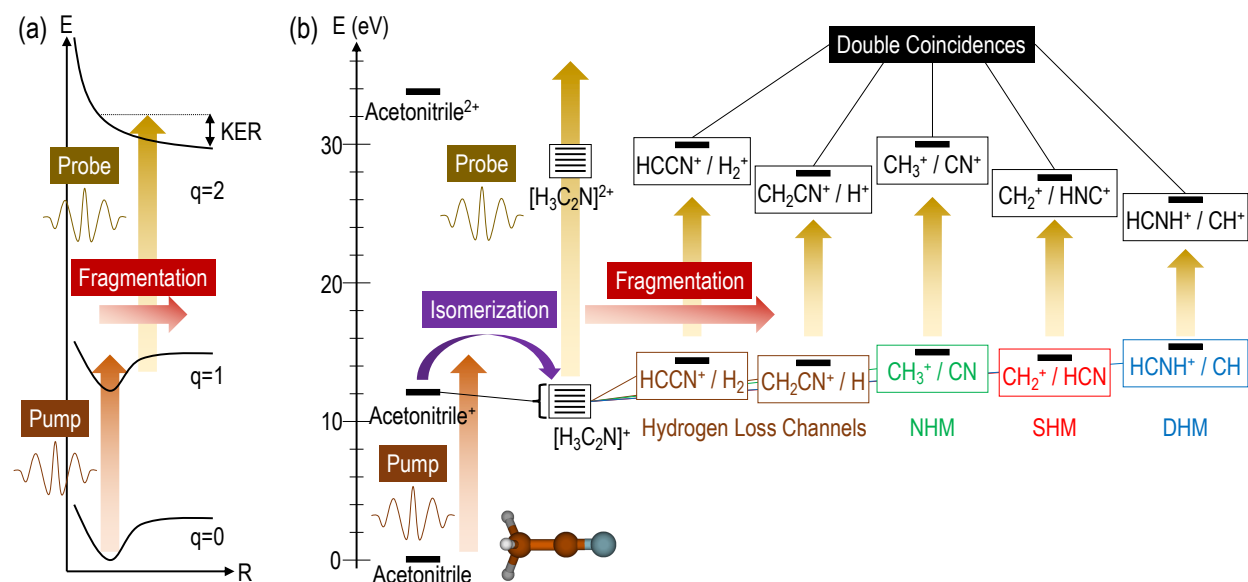


Figure S1: panel (a) shows the general scheme of the CEI technique via a pump-probe technique. Panel (b) shows the energy diagram for acetonitrile molecule along with the - H and H_2 loss, isomerization and fragmentation - in the cationic acetonitrile before double ionization. The singly and doubly charged parent leads to specific fragmentation channels including H and H_2 loss, NHM, SHM and DHM.

Theoretical Analysis

Quantum chemistry calculations were carried out using the density functional theory (DFT). Ab-initio molecular dynamics calculations (AIMD) were performed using the Atom-centered Density Matrix Propagation method (ADMP),^{S1-S4} employing the B3LYP (Becke’s three parameter non-local hybrid exchange potential^{S5} with the non-local correlation^{S6}) functional together with the 6-31++G(d,p) basis set. In the ADMP method, electronic structure is described quantum mechanically (in this case at the B3LYP/6-31++G(d,p) level) and the nuclear motion is assumed to be purely classical and is calculated on the fly by using the forces associated with the instantaneous potential created by the electrons. Following previous theoretical work on coupled electron and nuclear dynamics from excited states in molecules of this size (see, for example,^{S7-S13}), we assume, in this work, that the initial excitation energy has already been relaxed to the ground electronic state. This should be a reasonable approximation when the investigated migration dynamics are slower than the (non-adiabatic) internal conversion processes leading to such energy relaxation. There are cases where electronic relaxation through conical intersections can take much longer, up to a few picoseconds, in which case, molecular dynamics calculations including relaxation from electronically excited states are mandatory. However, the reasonable agreement between our results and the experimental findings suggest that we are not in this scenario. The simulations were performed for the singly-charged acetonitrile ions resulting from the vertical ionization. For each value of the excitation energy, randomly distributed among the nuclear degrees of freedom, 500 trajectories were computed. To ensure the adiabaticity of the dynamics, we have imposed a time step of $\Delta t = 0.1$ fs and a fictitious electron mass of $\mu = 0.1$ amu. The maximum propagation time was 2 ps. Inspired by the results obtained in the molecular dynamics simulations, we explored the potential energy surface of the singly-charged acetonitrile molecule at the same level of theory: B3LYP/6-31++G(d,p). In particular, we located critical points in the most relevant paths corresponding to H dissociation, isomerization, and fragmentation processes. Harmonic vibrational frequencies were

computed to characterize minima and transition states (TS) and intrinsic reaction coordinate (IRC) calculations (IRCs) to verify connectivity between TSs and adjacent minima. All the simulations have been carried out with the Gaussian16 program.^{S14}

Potential Energy Surface

Fig. S1 panel (a) presents the general scheme of the CEI technique while panel (b) illustrates the energy for ionization and for dissociation in the main channels in acetonitrile. In the main text a detailed exploration of the singly-charged potential energy surface is provided.

Molecular Dynamics

Table S1: Statistics of the ADMP simulations for singly-charged acetonitrile. The percentage of calculated trajectories for each channel at different excitation energies is listed.

Channel	Notation	5 eV	10 eV	15 eV
$\text{H}_3\text{C}_2\text{N}^+$		96.6	43.3	7.2
HC/ H_2CN^+	DHM	0.0	0.2	1.6
H/ $\text{H}_2\text{C}_2\text{N}^+$	H-diss	2.8	33.6	49.6
$\text{H}_2\text{C}^+/\text{HCN}$	SHM	0.0	4.6	5.2
$\text{H}_2/\text{HC}_2\text{N}^+$	H_2 -diss	0.4	15.0	9.6
$\text{H}_2^+/\text{HC}_2\text{N}$	H_2 -diss	0.2	2.4	8.0
$\text{H}_3\text{C}^+/\text{CN}$	NHM	0.0	0.6	0.4
3 fragments		0.0	0.2	18.4

We have performed molecular dynamics simulations in the singly-charged acetonitrile molecule considering three values of excitation energy: 5, 10 and 15 eV. 500 trajectories were computed up to 250 fs for each value of excitation energy. Those trajectories not showing fragmentation in the first 250 fs were extended up to a maximum propagation time of 2 ps. Statistics on the fragmentation channels are shown in Table S1. The calculated yields are in qualitative agreement with the experimental ones given in Table 1 of the main manuscript, especially for excitation energies around 10-15 eV. As in the experiment, our

MD calculations predict that H and H₂ losses are the dominant processes, followed by SHM and DHM, and finally NHM.

Analysis of the vibrational modes

To shed some light on the role of different vibrational modes in the isomerization and fragmentation processes, we have calculated the vibrational states of the cation and the neutral molecule in their ground states. The corresponding vibrational frequencies are given in Table S2.

Table S2: Vibrational frequencies for the neutral and singly-charged acetonitrile molecule. Mode characterization corresponds to the neutral molecule. Vibrational frequencies have been computed at the B3LYP/6-31++G(d,p) level of theory over the geometry previously optimized at the same level

Mode	$\nu_{\text{neutral}}(\text{cm}^{-1})$	$\nu_{\text{cation}}(\text{cm}^{-1})$
CH asymmetric stretching, ν_{CH}	3135.24	3131.26
CH asymmetric stretching, ν_{CH}	3135.24	2858.23
CH symmetric stretching, ν_{CH}	3057.98	2763.12
CN stretching, ν_{CN}	2364.27	2086.79
CH asymmetric bending, δ_{CH}	1478.23	1402.88
CH asymmetric bending, δ_{CH}	1478.23	1186.26
CH symmetric bending, δ_{CH}	1415.19	1075.59
CH ₃ rocking, ρ_{CH}	1060.27	1008.55
CH ₃ rocking, ρ_{CH}	1060.27	934.87
CC stretching, ν_{CC}	929.25	446.36
CH bending, δ_{CCN}	378.64	369.55
CCN bending, δ_{CCN}	378.64	191.83

Labeling of the different vibrational modes corresponds to the neutral molecule, for which there is no ambiguity. In contrast, the modes in the molecular cation are mixed and the characterization is not that straightforward. In general, they correspond to those in the neutral molecule with some contributions from other modes. The larger changes are observed for those modes where hydrogen atoms are involved. These modes are softened (redshifted), which further supports the fact that hydrogen migration is so efficient in the molecular cation.

Supplemental Experimental Analysis

H^+ / H_2^+ Dissociation

The Kinetic Energy Release (KER) as a function of probe pulse delay for the hydrogen dissociation channels is shown in the Supplemental Figure S2. Note that the constant band is centered around 4 eV, rather than the roughly 5.5 eV for the hydrogen migration channels shown in Fig.2 in the main text. We fit these figures following the same procedure as for the hydrogen migration channels: using a global fitting method and subtracting the constant band fit leaving only the dynamic, 1/R like behavior. The results of this fit are shown in Table 1 in the main text, and the details regarding the fit can be found below in the below section.

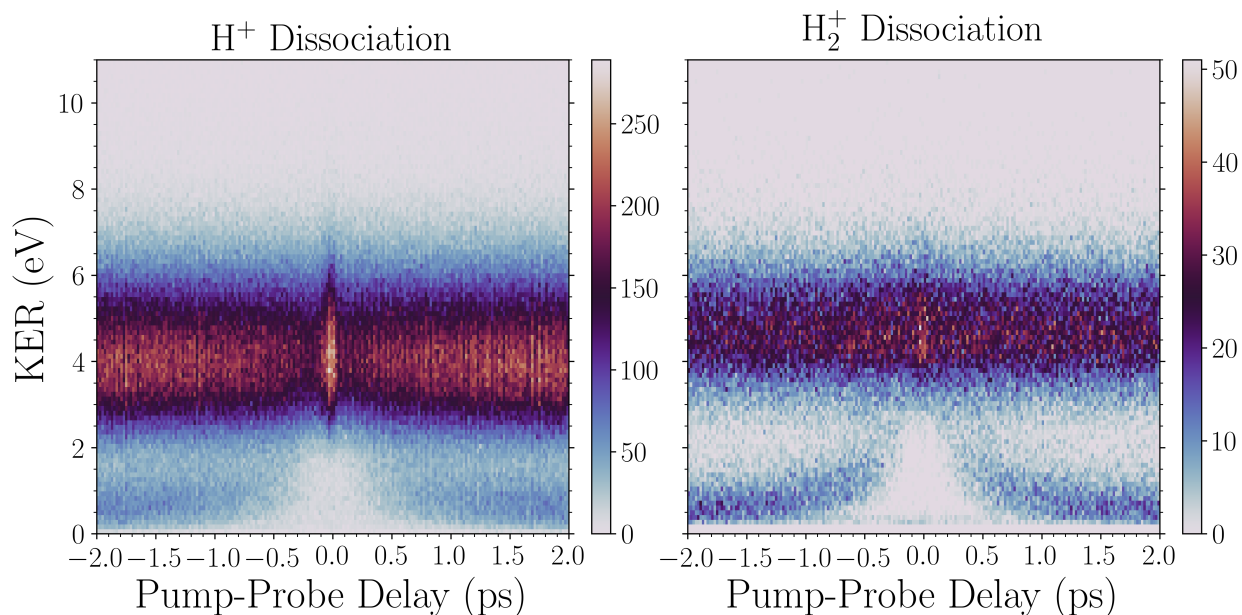


Figure S2: Kinetic Energy Release as a function of the probe pulse delay for H^+ and H_2^+ dissociation.

Global Fitting

To resolve the 1/R-like dynamic shown in the KER vs. pump-probe delay figures (e.g. Fig.S2), we employ a global fitting method. Since the data shows similar intensities and

timescales, the positive and negative pump-probe delay are folded about time zero to increase the statistics. We then fit the pump-probe delay slices with a function comprised of the sum of two main portions. The first part of this sum is the sum of a Gaussian and Cauchy distribution sharing a common central position, which was constrained to fit the static band. The other is the Fréchet distribution, which has been chosen for its long asymmetric tailing behavior that can be seen on the upper side of the $1/R$ component of the KER vs pump-probe delay plots. The Fitting of this sum uses a least squares method implemented by the python library script, utilizing the `curve_fit` implementation.

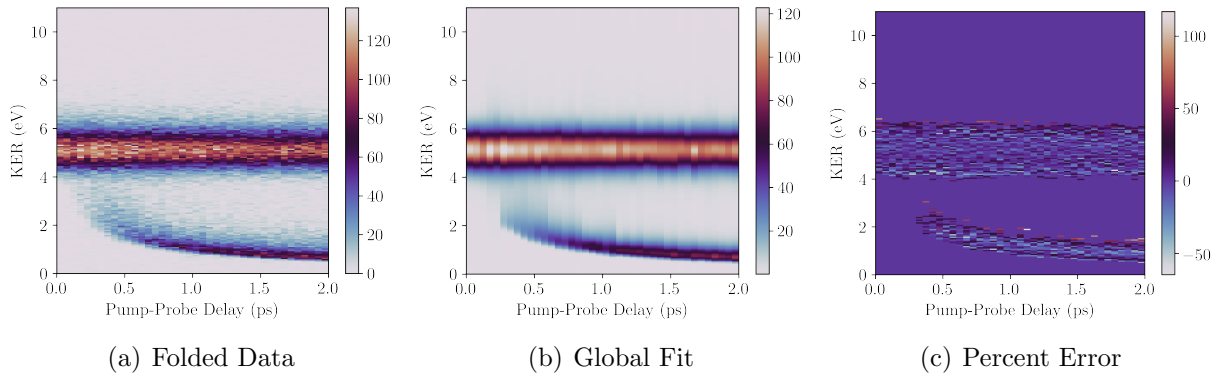


Figure S3: Raw NHM data folded around pump-probe delay = 0, the delay-sliced global fit, and the percent difference between them.

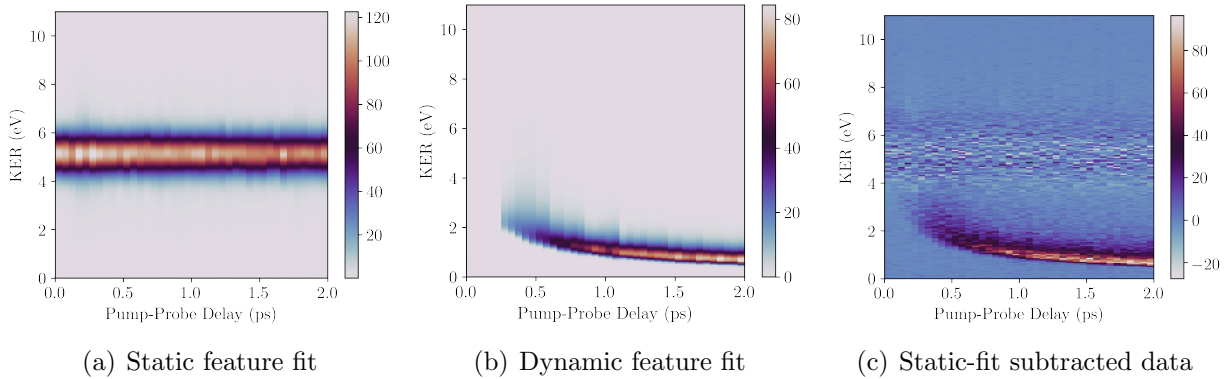


Figure S4: Static and $1/R$ features fit using global fit, and data with the static fit subtracted to retrieve only the $1/R$ feature on the collected data for the NHM.

The raw data and global fit for the NHM channel are visible in the Supplemental Fig. S3, as well as the percent difference between them. Supplemental Fig. S4 shows the static and

the $1/R$ portion of the fit separately for the same data, as well as the raw data with the static band fit subtracted from it. The Amplitude for the Gaussian fit to the static arm is roughly constant, thus the subtraction gives a reasonable representation of the channel dynamics. To get the time-constant τ for the population of the $1/R$ behavior, we project the subtracted data of Fig. S4(c) onto the pump-probe delay axis, and fit it with the function:

$$f(\Delta t) = \begin{cases} \text{background} & \Delta t < t_0 \\ A [1 - e^{-(\Delta t - t_0)/\tau}] + \text{background} & \Delta t \geq t_0 \end{cases} \quad (1)$$

where Δt is the pump-probe delay, A is a normalization constant, τ is the exponential time constant, and t_0 is the shift from time zero. An additional constant background noise is assumed. The function is fit, allowing the constants A , t_0 , τ , and background to vary. Physically, τ represents the breakup time and t_0 represents the time for isomerization. You can see this fitting for the SHM in Fig. S5

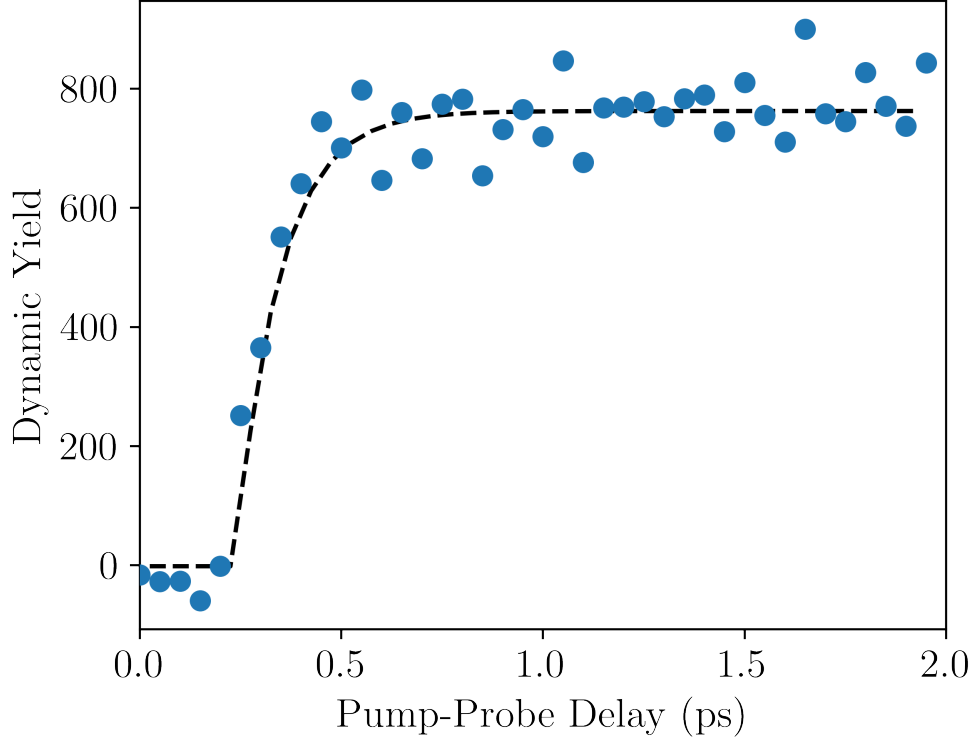


Figure S5: Least-squares fit of equation 1 for the static band subtracted NHM data projected onto the time axis.

Data Extraction

Identifying the correct dissociation channels begins by extracting the raw data recorded by the COLTRIMS, and plotting the time of flight (TOF) of all fragmented ions. Similar to most ion time-of-flight spectrometers, the arrival time is proportional to the $\sqrt{m/q}$ of the detected ion. After the TOF for the relevant fragmented ions of a particular breakup channel are identified (see Supplemental Fig.S6), we compare it to the photoion-photoion coincidence plot (PIPICO), which can be seen in Fig.S7. We then extract the negative-sloping distributions that correspond to the fragments we have identified. The PIPICO regions specific to hydrogen disassociation and hydrogen migration can also be seen in Fig. S7.

Once the events in the identified channels have been extracted, the momentum is calculated for every detected particle from the time of flight and position detection. We also

calculate the kinetic energy of each particle, and the kinetic energy release of the event, which is the sum of the kinetic energies of all fragment ions. There are some false-coincidences in the raw data, which can be seen by plotting the kinetic energy of the first detection vs the second in the channel corresponding to NHM. The expected trend line for KE2 vs KE1 would be $\sqrt{m_2/m_1}$, but as can be seen in the Supplemental figure 7, there are some non-physical events detected which are not considered since they do not satisfy momentum conservation, as shown in the Supplementary Fig. S8(c)

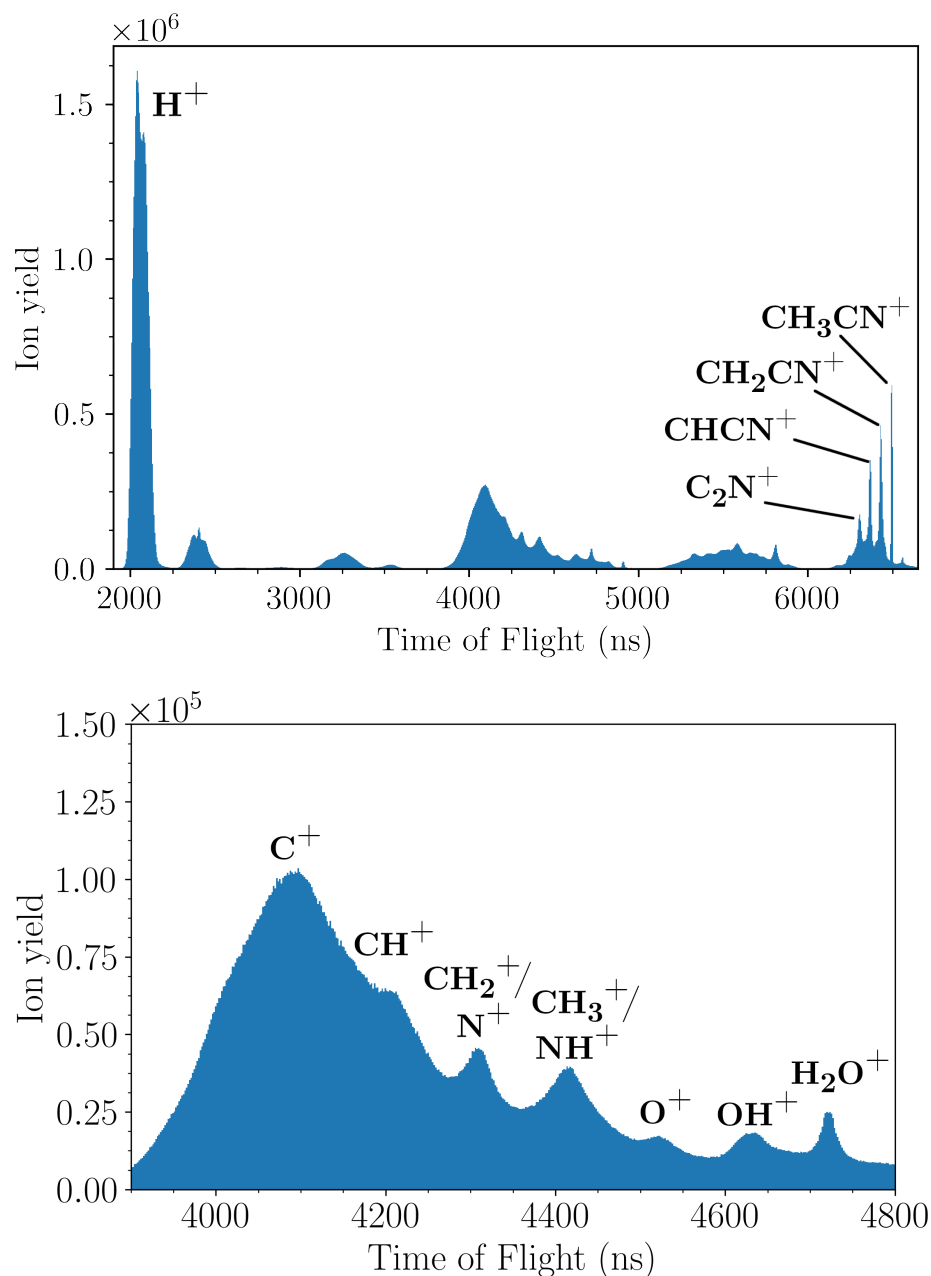


Figure S6: Raw time of flight spectrum for all particles observed in the COLTRIMS, in units of ns. The top figure displays the whole observed spectrum, where the peak on the left is H^+ , and the series of peaks at roughly 6300 ns is the parent molecule CH_3CN minus hydrogen ions. The bottom part is focused on the region of the fragmented ions corresponding to hydrogen migration (as well as the products of water contamination in the chamber).

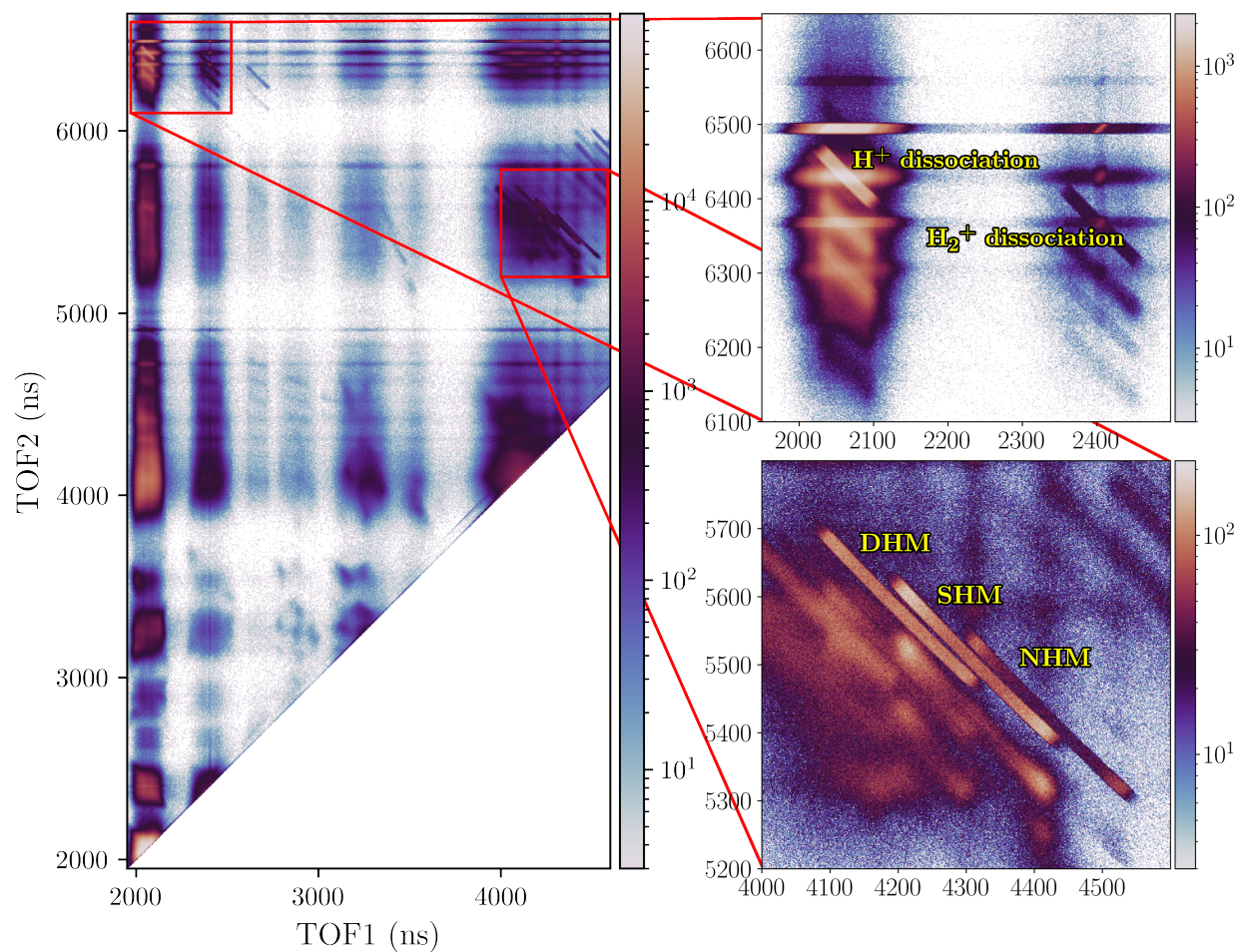


Figure S7: Photoion-photoion coincidence time-of-flight spectrum of CH_3CN . Two regions are highlighted: one containing H^+ and H_2^+ dissociation which can be seen on the top, and one containing the hydrogen migration channels on the bottom.

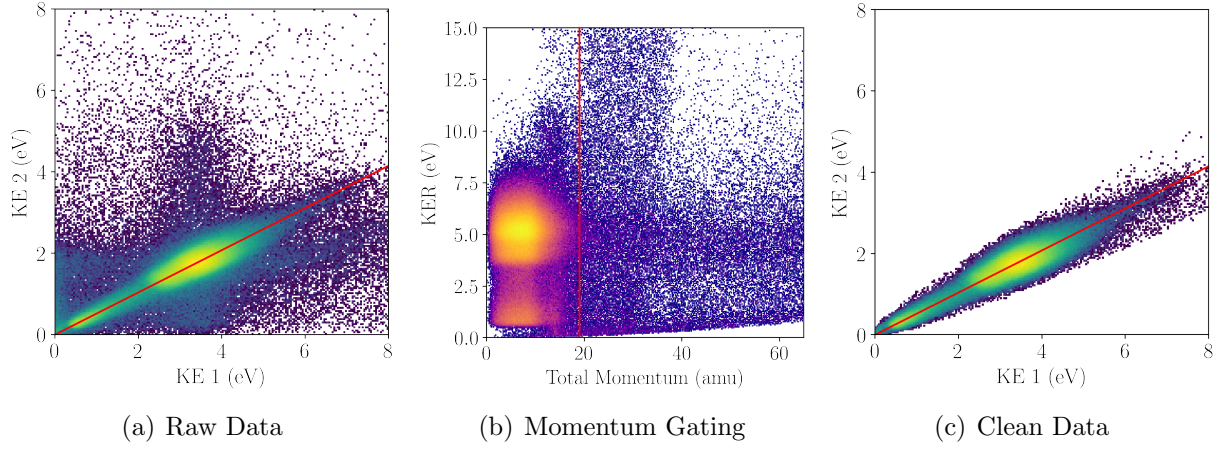


Figure S8: The kinetic energy of the two fragment ions for the SHM is plotted in the three figures above, with the red trend line in figure (a) and (c) being the kinematically expected $\sqrt{m_2/m_1}$. We gate the data keeping only those to the left of the red line in figure (b). The left only events, shown on the right, conserve momentum. All three above figures have log z-axis.

References

- (S1) Schlegel, H. B.; Millam, J. M.; Iyengar, S. S.; Voth, G. A.; Daniels, A. D.; Scuseria, G. E.; Frisch, M. J. Ab initio molecular dynamics: Propagating the density matrix with Gaussian orbitals. *J. Chem. Phys.* **2001**, *114*, 9758–9763.
- (S2) Iyengar, S. S.; Schlegel, H. B.; Millam, J. M.; A. Voth, G.; Scuseria, G. E.; Frisch, M. J. Ab initio molecular dynamics: Propagating the density matrix with Gaussian orbitals. II. Generalizations based on mass-weighting, idempotency, energy conservation and choice of initial conditions. *J. Chem. Phys.* **2001**, *115*, 10291–10302.
- (S3) Schlegel, H. B.; Iyengar, S. S.; Li, X.; Millam, J. M.; Voth, G. A.; Scuseria, G. E.; Frisch, M. J. Ab initio molecular dynamics: Propagating the density matrix with Gaussian orbitals. III. Comparison with Born–Oppenheimer dynamics. *J. Chem. Phys.* **2002**, *117*, 8694–8704.
- (S4) Iyengar, S. S.; Schlegel, H. B.; Voth, G. A. Atom-Centered Density Matrix Propagation (ADMP): Generalizations Using Bohmian Mechanics. *J. Phys. Chem. A* **2003**, *107*, 7269–7277.
- (S5) Becke, A. D. Density-functional thermochemistry. III. The role of exact exchange. *J. Chem. Phys.* **1993**, *98*, 5648–5652.
- (S6) Lee, C.; Yang, W.; Parr, R. G. Development of the Colle-Salvetti correlation-energy formula into a functional of the electron density. *Phys. Rev. B* **1988**, *37*, 785–789.
- (S7) Capron, M.; Díaz-Tendero, S.; Maclot, S.; Domaracka, A.; Lattouf, E.; Ławicki, A.; Maisonnay, R.; Chesnel, J.-Y.; Méry, A.; Pouilly, J.-C., et al. A Multicoincidence Study of Fragmentation Dynamics in Collision of γ -Aminobutyric Acid with Low-Energy Ions. *Chem.–Eur. J.* **2012**, *18*, 9321–9332.

- (S8) Maclot, S.; Piekarski, D. G.; Domaracka, A.; Mery, A.; Vizcaino, V.; Adoui, L.; Martín, F.; Alcamí, M.; Huber, B. A.; Rousseau, P., et al. Dynamics of glycine dications in the gas phase: ultrafast intramolecular hydrogen migration versus Coulomb repulsion. *J. Phys. Chem. Lett.* **2013**, *4*, 3903–3909.
- (S9) Piekarski, D. G.; Delaunay, R.; Maclot, S.; Adoui, L.; Martín, F.; Alcamí, M.; Huber, B. A.; Rousseau, P.; Domaracka, A.; Díaz-Tendero, S. Unusual hydroxyl migration in the fragmentation of β -alanine dication in the gas phase. *Phys. Chem. Chem. Phys.* **2015**, *17*, 16767–16778.
- (S10) Kukk, E.; Ha, D.; Wang, Y.; Piekarski, D. G.; Díaz-Tendero, S.; Kooser, K.; Itälä, E.; Levola, H.; Alcamí, M.; Rachlew, E.; Martín, F. Internal energy dependence in X-ray-induced molecular fragmentation: an experimental and theoretical study of thiophene. *Phys. Rev. A* **2015**, *91*, 043417.
- (S11) Maclot, S.; Delaunay, R.; Piekarski, D. G.; Domaracka, A.; Huber, B.; Adoui, L.; Martín, F.; Alcamí, M.; Avaldi, L.; Bolognesi, P., et al. Determination of energy-transfer distributions in ionizing ion-molecule collisions. *Phys. Rev. Lett.* **2016**, *117*, 073201.
- (S12) Piekarski, D. G.; Delaunay, R.; Mika, A.; Maclot, S.; Adoui, L.; Martín, F.; Alcamí, M.; Huber, B. A.; Rousseau, P.; Díaz-Tendero, S., et al. Production of doubly-charged highly reactive species from the long-chain amino acid GABA initiated by Ar^{9+} ionization. *Phys. Chem. Chem. Phys.* **2017**, *19*, 19609–19618.
- (S13) Kling, N. G.; Díaz-Tendero, S.; Obaid, R.; Disla, M.; Xiong, H.; Sundberg, M.; Khosravi, S.; Davino, M.; Drach, P.; Carroll, A., et al. Time-resolved molecular dynamics of single and double hydrogen migration in ethanol. *Nat. Commun.* **2019**, *10*, 1–8.
- (S14) Frisch, M. J.; Trucks, G. W.; Schlegel, H. B.; Scuseria, G. E.; Robb, M. A.; Cheeseman, J. R.; Scalmani, G.; Barone, V.; Petersson, G. A.; Nakatsuji, H.; Li, X.;

Caricato, M.; Marenich, A. V.; Bloino, J.; Janesko, B. G.; Gomperts, R.; Men-
nucci, B.; Hratchian, H. P.; Ortiz, J. V.; Izmaylov, A. F.; Sonnenberg, J. L.; Williams-
Young, D.; Ding, F.; Lipparini, F.; Egidi, F.; Goings, J.; Peng, B.; Petrone, A.;
Henderson, T.; Ranasinghe, D.; Zakrzewski, V. G.; Gao, J.; Rega, N.; Zheng, G.;
Liang, W.; Hada, M.; Ehara, M.; Toyota, K.; Fukuda, R.; Hasegawa, J.; Ishida, M.;
Nakajima, T.; Honda, Y.; Kitao, O.; Nakai, H.; Vreven, T.; Throssell, K.; Mont-
gomery, J. A., Jr.; Peralta, J. E.; Ogliaro, F.; Bearpark, M. J.; Heyd, J. J.; Broth-
ers, E. N.; Kudin, K. N.; Staroverov, V. N.; Keith, T. A.; Kobayashi, R.; Normand, J.;
Raghavachari, K.; Rendell, A. P.; Burant, J. C.; Iyengar, S. S.; Tomasi, J.; Cossi, M.;
Millam, J. M.; Klene, M.; Adamo, C.; Cammi, R.; Ochterski, J. W.; Martin, R. L.;
Morokuma, K.; Farkas, O.; Foresman, J. B.; Fox, D. J. Gaussian16 Revision C.01.
2016; Gaussian Inc. Wallingford CT.